PHYSICAL REVIEW B **106**, 014108 (2022)

Melting curve and transport properties of ammonia ice up to the deep mantle conditions of Uranus and Neptune

Zhao-Qi Wang,[1,*] Jia-Jin Tan,[2] Xiang-Rong Chen,[3] Zheng-Xin Yan,[1] Wei Liu,[1] Yi-Xian Wang,[1]
Gao-Liang Zhou,[1] Ke-Zhao Xiong,[1] and Xin-Lin Song[1]
[1]*College of Science, Xian University of Science and Technology, Xian 710054, People's Republic of China*
[2]*College of Science, East China University of Technology, Nanchang 330013, People's Republic of China*
[3]*College of Physics, Sichuan University, Chengdu 610065, People's Republic of China*

(Received 6 May 2022; accepted 13 July 2022; published 25 July 2022)

Motivated by the poor knowledge of the implication of planetary ice on the internal convection and anomalous magnetic field of ice giants, we perform extensive first-principles molecular dynamics simulation on ammonia ice to investigate its thermophysical behaviors at high temperature (T) and pressure (P) conditions relevant to the deep mantle of Neptune and Uranus. The melting curve, transport properties, and sound velocity of ammonia up to 350 GPa and 5500 K, spanning from fluid mixtures to a highly compressed superionic regime, are determined. A first-order phase transition of ammonia from the plastic state to the superionic state is observed explicitly, which is associated with the reduction of entropy. In contrast to previous predictions, the melting curve elucidates the existence of superionic ammonia in deep planetary interiors. Inspection of the reduction for transport properties and sound velocity along the isentrope of ice giants further evidences that superionic ammonia can sufficiently sustain the planetary dynamo mechanism and may contribute to the internal stratification which is responsible for the generation of the multipolar magnetic field. Finally, a comprehensive phase diagram of ammonia extended to a higher T-P regime is constructed, which provides a clear picture for studying the fundamental behavior and phase transition of ammonia in deep planets, and enhances our understanding of the interior structure and thermal convection of these planetary systems.

DOI: 10.1103/PhysRevB.106.014108

I. INTRODUCTION

As the major constituent for the deep interiors of Neptune, Uranus [1–3], and exoplanets [4,5], the thermophysical behaviors of ammonia ice under high temperature (T) and pressure (P) are of particular importance for modeling the planetary science and designing the laboratory astrophysics. Depending on the size of these bodies, the estimated T and P of Neptune and Uranus span from 2000 K and 20 GPa at the upper ice mantle boundary, up to about 7000 K and 600 GPa at the core-mantle boundary [6,7]. Under such dense conditions, ammonia exhibits polymorphism and has a rich phase diagram, including fluid [8,9], plastic [10], superionic [1,11,12], and ionic-crystal phases [13–15]. Among them, superionic ammonia, in which the molecular nature disappears and protons rapidly diffuse almost freely through nitrogen sublattices, is regarded as one of the critical candidates to form the multipolar magnetic fields by the planetary dynamo in a thin convective layer of Neptune and Uranus [1,3]. Revealing the nature of these diverse behaviors at deep planetary conditions is indispensable for understanding the observable properties (magnetic field and gravitational moments) and constructing the interior model of these ice giants.

Until very recently, the high T-P responses of ammonia have been measured extensively by convergent explosives [16], gas gun facilities [3,17–19], diamond anvil cell (DAC) [11–14,20–23], and pulsed-power lasers [8]. These measurements have provided considerable insight over the past few decades. Most experiments on solid ammonia [11–14,20,21,23,24] have been devoted to confirming the phase transition and determining the melting line and phase diagram. However, the melting line of ammonia has been limited to 62 GPa and 3336 K (see Fig. 1), and three recent attempts [12,21,23] aiming at verification of the melting temperature of ammonia at above 43 GPa have provided contradictory conclusions, making definitive experimental confirmation of superionic state elusive. Meanwhile, the stability and transport properties of ammonia along the isentrope of ice giants remain ambiguous due to the absence of available high T-P phase diagrams relevant to the deep mantle condition. As a result, we cannot determine whether the convection of Neptune and Uranus involves the superionic region. Experimental realizations of liquid ammonia [3,8,16–19,22] usually focused on the measurements of the Hugoniot and electronic conduction up to 350 GPa and 40000 K, which are far higher than the isentropic condition of ice giants (see Fig. 1). We thus struggle to resolve well the dynamo process and magnetic field of these planetary systems [6]. These discrepancies have not been solved in previous theoretical research [25,26], underlining the need for additional investigations to bridge the gap between static and dynamic investigations, and to explore the nature of abnormal behaviors in these ice planets and their large satellites.

---

[*] zhqwangsc@foxmail.com

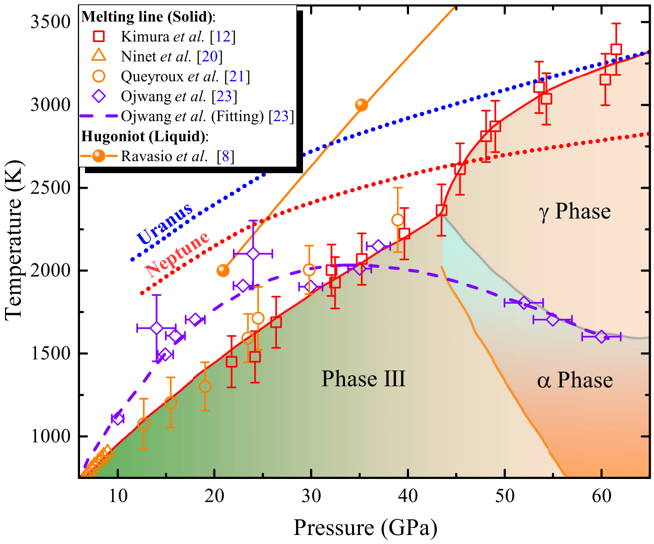

FIG. 1. The P-T phase diagram of ammonia. The open triangles and circles represent the melting line of solid ammonia obtained by the DAC with the resistive heating techniques [20] and Raman measurements [21], respectively. The blue diamonds and dashed line are the melting curve of Ojwang *et al.* [23] inferred from their Raman study. The red squares and phases (such as phase III, α, and γ) are taken from the Ref. [12] determined by the Brillouin spectroscopy. The Hugoniot of liquid ammonia [8] and the planetary isentrope of Neptune and Uranus [7] are also shown for comparison.

Therefore, in this paper, we perform extensive first principles molecular dynamics (FPMD) simulations to extend the theoretical determination of the melting curve and phase diagram of ammonia to a higher T-P regime equivalent to that in the deep mantle of planetary interiors. The transport and elastic properties along the isentrope of Neptune and Uranus up to 350 GPa and 5500 K enable us to clarify the contradiction between previous experiments and to judge the contribution of ammonia to the peculiar magnetic field.

II. COMPUTATIONAL METHODS

FPMD simulations are performed using the Vienna *ab initio* simulation package [27] code with the strongly constrained and appropriately normed [28] exchange-correlation functional. The simulations are implemented for a canonical ensemble, together with the ionic temperature controlled by the Nosé-Hoover thermostat [29] and the electronic temperature dominated by the Fermi-Dirac distribution [30]. The supercell contains 108 ammonia molecules and the wave function is expanded up to the cutoff energy of 1000 eV. The periodic boundary condition is enforced and the Brillouin zone sampling is performed at the Γ point only. We run for 20 000 steps at each density-temperature condition and the time step takes on values of 0.5–1.0 fs with smaller values corresponding to higher temperatures. The total simulation time is up to 10–20 ps, then the first 2–3 ps is used for thermalization and the last 8–17 ps is used for averaging the thermodynamic quantities, which is found to be sufficient for the convergence of the computed energies, pressures, and transport coefficients. In addition, the nuclear quantum effects of the system are taken into account by the vibrational frequency spectrum of ammonia [10,31]. More details about the computational methods, convergence tests, and representative signals are available in the Supplemental Material [32].

III. RESULTS AND DISCUSSIONS

The melting curve of solid ammonia is determined by the FPMD simulations with the Z method. The simulation interval of the temperature is 200 K along each isochore and the melting point is considered to be the average of both sides of the discontinuity for the temperature and pressure. The melting temperatures of our results up to 350 GPa and 5100 K are shown in Fig. 2(a), together with the available DAC experimental data [12,20,21] up to 62 GPa. The solid region of ammonia in our proposed melting curve is extended to higher temperature than previous research [1,26] and the boundary line above 45.16 GPa and 2400 K rises faster. This discontinuity is favored by the recent experimental observations [12,21], but deviates from the negative slope reported by Ojwang *et al.* [23] in the ranges of 35–60 GPa and 1600–2000 K. According to the Clausius-Clapeyron relation, $\Delta T/\Delta P = \Delta V/\Delta S$, the sudden increase in the slope of the melting line is perhaps associated with the first-order phase transition from the plastic state to superionic state, as discussed later. Therefore, to capture the shape of the melting curve, we use the I-II-fluid triple point (P_0 = 0.307 GPa and T_0 = 217.34 K [37]) and plastic-superionic-fluid triple point (P_0 = 45.16 GPa and T_0 = 2400 K) of ammonia as reference points to fit separately our data below and above 45.16 GPa using the Simon-Glatzel equation [38],

$$T_m = T_0 \times [(P_m - P_0)/a + 1]^{1/b}, \tag{1}$$

where T_m and P_m are the temperature and pressure of the melting curve. The best-fit parameters determined from a nonlinear least-squares analysis (the correlation coefficient of fitting is larger than 99%) below 45.16 GPa yield a = 1.06 ± 0.06 GPa and b = 1.57 ± 0.03, which are in excellent agreement with the previous experiments [12,20,21] within their stated uncertainty, and those above 45.16 GPa yield a = 2.80 ± 0.31 GPa and b = 6.16 ± 0.17. This consistency between our results and recent experiments indicates that the selected parameters in our FPMD simulations can reasonably reproduce the melting temperatures, which lays a solid foundation for reliably predicting the following transport and elastic properties of ammonia.

For comparison, the melting behaviors of other possible planetary materials (such as He [33], $HeNH_3$ [10], CH_4 [34], and H_2O [31,35]) that make up the deep interior of ice giants are displayed in Fig. 2(b). The isentrope of Neptune and Uranus constructed by the planets' gravity fields, shape, rotation periods, and equation of state is taken from Ref. [7]. We find that the melting curve of He and $HeNH_3$ are far below the isentrope of ice planets, evidencing that the insertion of helium substantially reduces the temperatures at which solid states can be formed relative to pure ammonia. The melting curve of water does not intersect with the isentrope of Neptune and Uranus below 90 and 145 GPa, respectively, and hence, H_2O should remain in the liquid state on top of upper ice mantle. Unlike water, the melting curve of ammonia is always

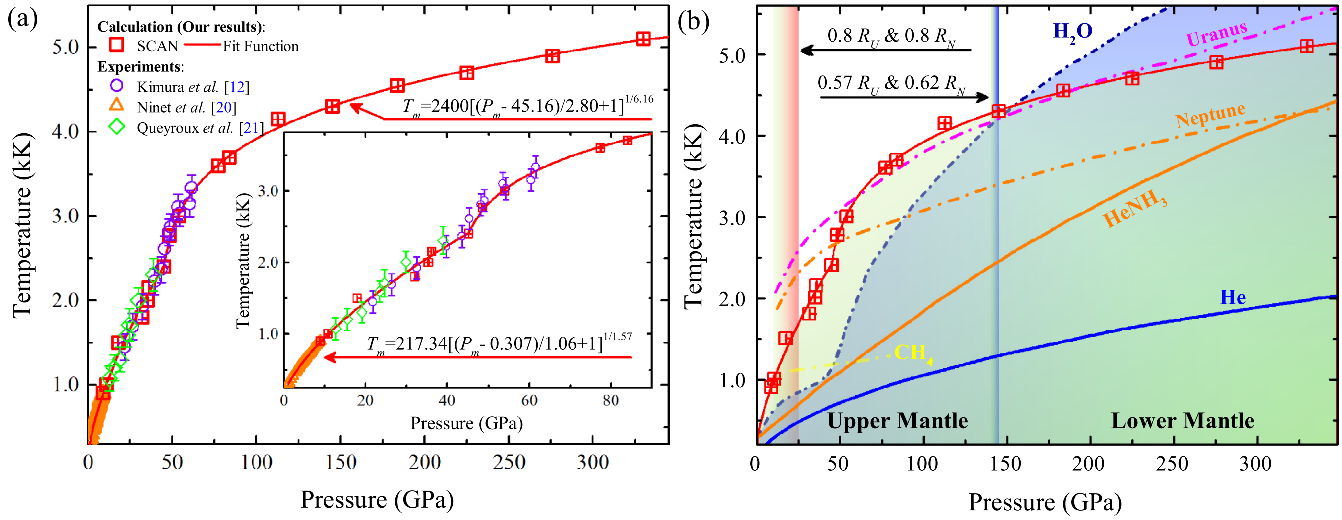

FIG. 2. Melting curve of ammonia and other planetary materials. (a) The melting points of our results (red squares) and previous DAC experimental data of Kimura *et al.* [12] (green diamonds), Ninet *et al.* [20] (orange triangles), and Queyroux *et al.* [21] (blue circles). The red solid line is the melting curve of NH_3 fitted by the Simon-Glatzel equation. (b) The melting line of NH_3 is compared to that of He [33] (blue solid line), $HeNH_3$ [10] (orange solid line), CH_4 [34] (yellow dashed line), and H_2O [31,35] (royal dashed line). The vertical lines mark the location of the upper and lower mantle of ice planets, where R_N and R_U are the planetary radius of Neptune and Uranus [36], respectively.

higher than the isentrope of Neptune above 48 GPa and nears the isentrope of Uranus within the pressure range of 60–350 GPa. This contrasts with previous predictions [1,26] that above 3000 K the melting line becomes very flat and never crosses the planetary isentropes. The higher melting temperature and discontinuity behavior of ammonia and water [35,39] are quite distinct from those of pure methane, which means that the intermolecular interactions, i.e., hydrogen bonds, may be one of the important factors to promote the structural stability of the former. From the estimated temperature-radius relationship for these planets [36], our calculations predict that liquid ammonia stably exists in the upper thin-shell zone of (0.8–0.75)R_N and (0.8–0.68)R_U, where R_N and R_U are the total radius of Neptune and Uranus, respectively. The solid ammonia appears in the lower mantle of Neptune ($R < 0.62$ R_N) and Uranus ($R < 0.57$ R_U). To identify the stability and convection of ammonia in the deep mantle, we further study its structural, transport, and elastic properties.

Figure 3 illustrates the evolution of the averaged coordination number (CN), conductivity (σ), diffusion (D), and viscosity coefficients of ammonia as a function of pressure along the isentrope of Neptune and Uranus. The CN in Fig. 3(a) is determined by integrating $4\pi r^2 \rho g_{\alpha\beta}(r)$ ($\alpha\beta$ = NH and NN) up to the first minimum of pair distribution function (PDF) $g_{\alpha\beta}(r)$ (see Fig. S1 [32]), where ρ is the number density of atoms. It is seen that, with the increase of pressure, CN_{NH} slowly increases from 2.72 at 11.34 GPa to 5.02 at 334 GPa, whereas CN_{NN} first increases to the maximum of 13.6 at 42 GPa and then decreases gradually to 11.93 at 334 GPa. This is because ammonia does not preserve in its molecular form at lower *T-P* regime, and it actually transforms into a liquid mixture of NH_3, H_2, and N_2 (see Fig. S1 [32]). With the increase of pressure and temperature, liquid mixtures rapidly dissociate and then transform into a solid state where the H_2 and N_2 disappear. The CNs of NN are compatible with those reported in the neutron-diffraction study (CN=14 [40]) and recent x-ray diffraction measurement (CN=12.7–14.1 [21]), and close to the expected CN of a close-packed structure (CN=12) but far from the bcc lattice (CN=8). This suggests a crucial clue that ammonia exhibits sensibly different structural information from that of general solid phase at above 42 GPa.

The electronic (σ_e) and ionic (σ_p) conductivity of ammonia in Fig. 3(b) have an obvious reduction at 42 GPa and then continue to increase rapidly to very high pressures, confirming this difference again. In combination with the conductivity, mean-square displacement (MSD), and atomic trajectories, we identify that ammonia enters into the superionic state above 42 GPa and this kink is a mark of a first-order phase transition from the fluid to superionic phase along the isentropes. In theory, electrical conductivity in the relatively shallow ice layer on the order of 10 S/cm is necessary to sustain the planetary dynamo mechanism for the generation of a multipolar magnetic field [1]. Our conductivities are larger than this threshold and reach $\sim 10^3$ S/cm at around 220 GPa, which are very coherent with those of ice XVIII (3×10^2 S/cm at 4000 K and 200 GPa) [41]. Thus, the superionic ammonia is capable of sufficiently dominating such a dynamo process and might contribute substantially to the deep mantle thermal convection in the ice giants. The electronic density of states (see Fig. S2 [32]) obtained from the HSE06 functional favors the presence of this superionic state, and predicts the closure of the electronic band gap at 42 GPa and 3000 K. The metallization in the fluid state is induced by molecular dissociation-ionization, and that in the superionic state is derived from the delocalized proton. This may lead to at least two consequences. First, the dynamo generation of the magnetic field should include the contribution of the higher electronic conductivity due to the metallization of ammonia and the lower ionic conductivity

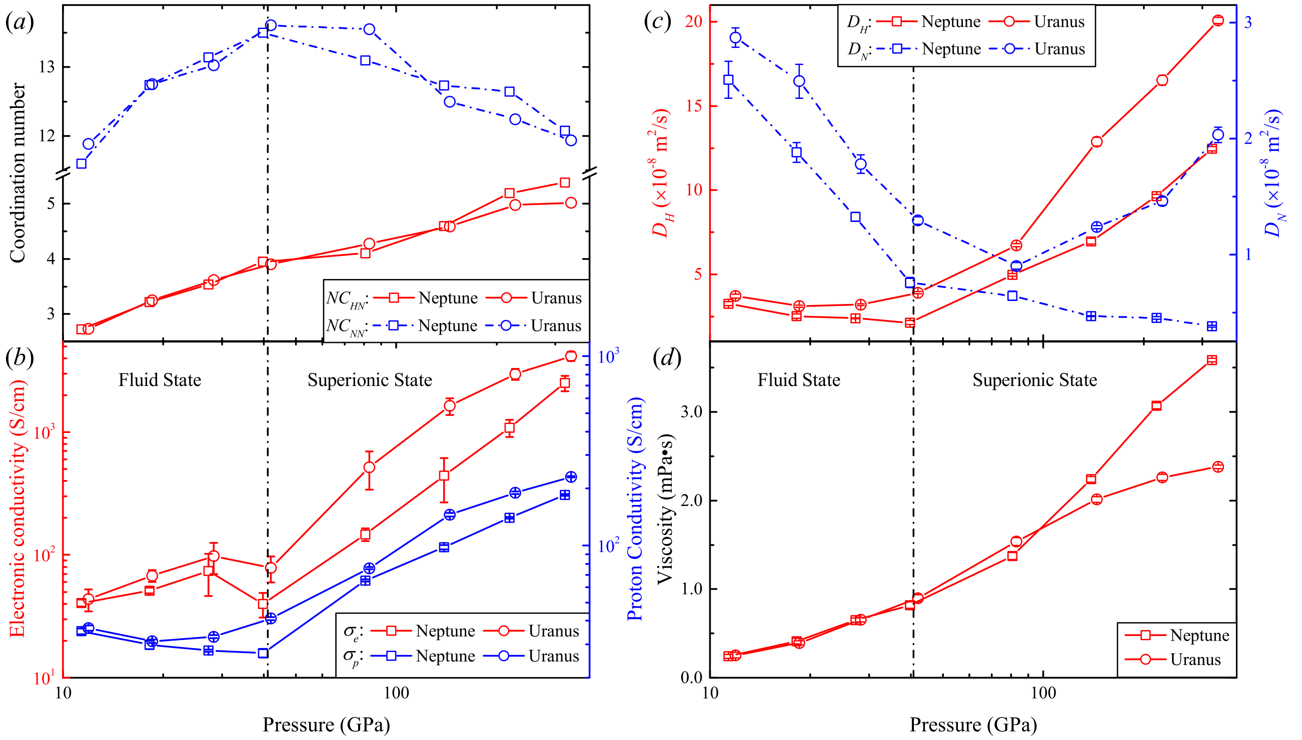

FIG. 3. The structural and transport parameters of ammonia along the isentrope of Neptune and Uranus, including (a) the averaged *NC* of HN and NN, (b) the electronic (σ_e) and ionic (σ_p) conductivity of ammonia, (c) diffusion coefficient of hydrogen (D_H) and nitrogen (D_N), and (d) viscosity coefficient of ammonia. Vertical dashed lines denote the phase transition from the fluid state to the superionic state.

due to the free diffusion of protons. Second, a metallic state of ammonia may affect its solubility with water and other planetary materials, which perhaps alters current views on the partitioning of these materials in the deeper regions of the ice layer.

Next we give the diffusion and viscosity coefficient of ammonia. In Fig. 3(c), the diffusion coefficient of hydrogen and nitrogen is denoted by D_H and D_N, respectively. The superionic regime is characterized by a transition from high values of D_H corresponding to higher compression, to small values of D_H corresponding to the low compression. Along the isentropes, the proton diffusion rate has a plateau in the liquid phase, shows a sharp rise in the superionic phase, and reaches $\sim 10^{-7}$ m^2/s at around 220 GPa and 4000 K, which is comparable to that of ice XVIII at similar conditions [41,42]. The viscosity of ammonia in Fig. 3(d) increases by a factor of 10 from the top layer of the upper mantle to lower mantle, which is remarkably consistent with the other planetary materials [9,36]. It signifies that the flow of superionic ammonia is likely to be more similar to that of slow convection within the solid ice mantle than to that of rapid swirls of fluid materials in the planetary interior. We also note the following features: (1) The D_N in Neptune gradually decreases to 0, whereas that in Uranus exhibits a minimum value at 83.3 GPa. (2) The D_N and D_H in Uranus are higher than those in Neptune, whereas the viscosities along the isentrope of Uranus are lower than those of Neptune at deeper condition. These differences can be interpreted as a consequence of the fact that the isentrope of Uranus is slightly higher than the melting line of ammonia, while that of Neptune is beneath it.

A combination of the proton fluid and the nitrogen lattice in the superionic phase raises the question of the characteristics of this hybrid phase, especially with respect to its response to electromagnetic stress, we therefore calculate the sound velocity of ammonia along the isentrope of Neptune in the same manner as Hernandez [43] and Millot [35], as displayed in Fig. 4. Note that no shear sound velocity can be detected in a homogeneous liquid and the longitudinal sound velocity should be equal to the bulk sound velocity. One can find that the longitudinal sound velocity increases with the increasing pressure up to the deep mantle and a discontinuity is observed at 48 GPa. This implies that the superionic ammonia has different longitudinal-wave propagation characteristics from the liquid phase and Neptune has a high-velocity layer at lower $0.75R_U$. In contrast to the previous conjecture, the obtained elastic responses of superionic ammonia (see Fig. S5 and Table S1 [32]) are comparable to those of the superionic water with X phase [35,41,43] at similar conditions. Thus, the deduction in the recent experiment [12] that the superionic ammonia may not contribute to the internal stratification is insufficient. Previous research [31,35,36] predicted that the magnetic fields of ice planets require highly electrically conducting regions and may be induced by the superionic state of planetary ice in a relatively shallow nonconvective layer. Considering the existing states, transport coefficients, and sound velocity of ammonia in the ice mantle, we deem that the superionic ammonia is capable of inducing the internal stratification for generating such multipolar magnetic fields. The reasons are as follows: (1) Compared with the superionic water, superionic ammonia can exist stably in the shallower

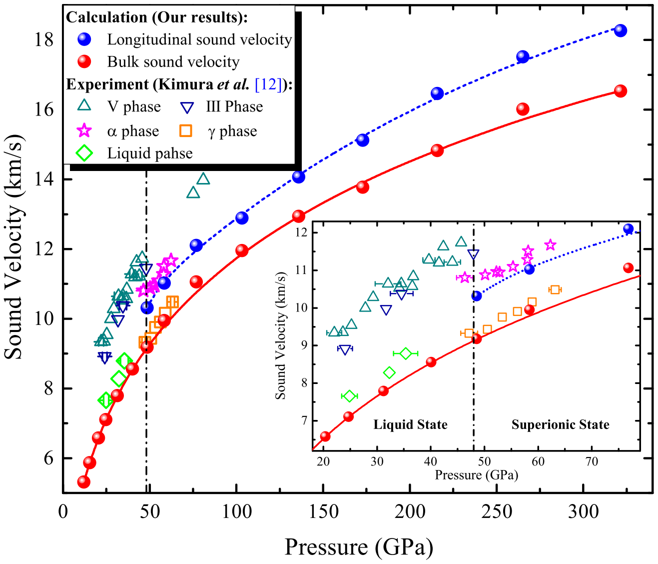

FIG. 4. The longitudinal and bulk sound velocity of ammonia as a function of the pressure along the isentrope of Neptune. The sound velocities measured by the Brillouin scattering [12] are shown for comparison. Lines are guides to the eye.

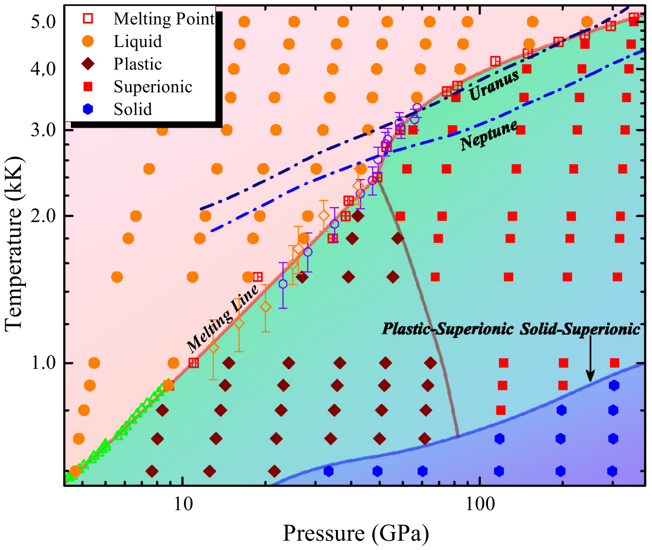

FIG. 5. Proposed high *P-T* phase diagram for ammonia compared with the planetary interior condition of Neptune (blue dashed line) and Uranus (navy dashed line) [7]. The simulation results are marked with four different solid symbols: liquid (orange circles), plastic (wine diamonds), superionic (red squares), and solid (blue hexagons) state. The melting curve of ammonia is obtained from our FPMD simulations (red squares) and previous DAC experiments (green triangles, blue circles, and orange diamonds) [12,20,21]. The plastic-superionic and solid-superionic phase boundaries are marked by the wine and blue lines, respectively.

layer of these ice planets. (2) The conductivity of superionic ammonia can sufficiently sustain the planetary dynamo processes. (3) The discontinuity of longitudinal sound velocity confirms the apparent difference between liquid and superionic ammonia, which is related to the stratification inside the ice planets.

Motivated by the poor understanding of the dynamical behaviors of the ammonia ice under high *T-P* condition, we use the MSD, PDF, and the atomic trajectories extracted from our FPMD simulations to identify specifically the polymorphism of ammonia and to construct a comprehensive phase diagram. Since the accuracy of theoretical prediction depends on the selected exchange-correlation functional, this phase diagram may need to be further verified in the future experiments. Figure 5 displays the final states of these simulations up to 360 GPa and 5500 K by distinguishing the fluid phase with positive D_H and D_N from the solid phase in which $D_N = 0$, and the superionic regime is characterized by positive D_H whereas $D_H = 0$ in the plastic regime. Solid lines are fitted from the boundary points of each type of atomic motion which divide the phase diagram into four regions: fluid, plastic, superionic, and solid. Inspired by the plastic state in the helium-ammonia system [10], we explore the possible plastic regime of the pure ammonia at low pressure. As expected, we find that the solid ammonia enters a plastic state around 20–65 GPa, in which hydrogen atoms rotate around the fixed nitrogen atoms, as shown in the MSD and atomic trajectory in Fig. S6 [32]. The crucial signature of the plastic phase is a finite MSD with a plateau at a quite low value, and the D_H in the plastic phase is about an order of magnitude lower than that in the superionic phase. The PDF in Fig. S7 [32] supports the distinction of the plastic and superionic state, and the hydrogen atoms in the former look liquidlike. Inspection of the PDF also indicates that the protons in superionic ammonia still maintain a strong interaction with the periodic nitrogen sublattice and the extra entropy of liquidlike protons may enhance the structural strength with the increase of diffusion rate, which provides an explanation on the elastic stiffening of ammonia along the isentrope of Neptune. Note that this paper is mainly focused on clarifying the contradiction about previous researches of ammonia along the isentrope of ice giants, therefore the α-γ phase transition of superionic ammonia reported by Kimura *et al.* [12] goes far lower than the scope of the present paper, which will be discussed in our following research.

IV. CONCLUSION

Extensive FPMD simulations are conducted to determine the melting curve, ionic structures, transport properties, and sound velocity of ammonia at conditions relevant to the deep mantles of Neptune and Uranus. Observation of the melting temperature and ionic structure reveals a first-order phase transition from the plastic state to the superionic state at 45.16 GPa and 2400 K attributed to the reduction of entropy. The melting curve of ammonia crosses with the isentrope of Neptune and nears the isentrope of Uranus, elucidating that ammonia mainly exists in the form of a fluid mixture phase in the top layer of the ice mantle and in the form of a superionic phase in the deep interior of ice giants. Discovery of reduction for the transport properties and sound velocity of ammonia along the isentrope of ice giants further indicates that the superionic ammonia could be stable up to pressure as high as 350 GPa and may have significant implications for the formation and evolution process of the magnetic field. Finally, a phase diagram of ammonia, including the solid, liquid, plastic, and superionic phases, is extended to the higher *T-P* condition. Our results not only successfully clarify the contradiction between previous experiments and ascertain the contribution of ammonia to the magnetic field but also shed more light on the mantle convection and dynamo modeling of these planets.

ACKNOWLEDGMENTS

This work is supported by the Doctoral Scientific Research Foundation of Xian University of Science and Technology (Grant No. 2050122007) and the National Natural Science Foundation of China (Grants No. 12074274, No. 11664002, and No. 11904282). This work is also supported by the TianHe-2 in the Shanxi Supercomputing Center of China.

[1] C. Cavazzoni, G. L. Chiarotti, S. Scandolo, E. Tosatti, M. Bernasconi, and M. Parrinello, Science **283**, 44 (1999).

[2] W. B. Hubbard, W. J. Nellis, A. C. Mitchell, N. C. Holmes, S. S. Limaye, and P. C. McCandless, Science **253**, 648 (1991).

[3] W. J. Nellis, D. C. Hamilton, N. C. Holmes, H. B. Radousky, F. H. Ree, A. C. Mitchell, and M. Nicol, Science **240**, 779 (1988).

[4] T. Guillot, Science **286**, 72 (1999).

[5] L. Zeng, S. B. Jacobsen, D. D. Sasselov, M. I. Petaev, A. Vanderburg, M. Lopez Morales, J. Perez Mercader, T. R. Mattsson, G. Li, M. Z. Heising, A. S. Bonomo, M. Damasso, T. A. Berger, H. Cao, A. Levi, and R. D. Wordsworth, Proc. Natl. Acad. Sci. USA **116**, 9723 (2019).

[6] R. Helled, N. Nettelmann, and T. Guillot, Space Sci. Rev. **216**, 38 (2020).

[7] N. Nettelmann, R. Helled, J. J. Fortney, and R. Redmer, Planet. Space Sci. **77**, 143 (2013).

[8] A. Ravasio, M. Bethkenhagen, J. A. Hernandez, A. Benuzzi-Mounaix, F. Datchi, M. French, M. Guarguaglini, F. Lefevre, S. Ninet, R. Redmer, and T. Vinci, Phys. Rev. Lett. **126**, 025003 (2021).

[9] R. Chau, S. Hamel, and W. J. Nellis, Nat. Commun. **2**, 203 (2011).

[10] C. Liu, H. Gao, A. Hermann, Y. Wang, M. Miao, C. J. Pickard, R. J. Needs, H. T. Wang, D. Xing, and J. Sun, Phys. Rev. X **10**, 021007 (2020).

[11] S. Ninet, F. Datchi, and A. M. Saitta, Phys. Rev. Lett. **108**, 165702 (2012).

[12] T. Kimura and M. Murakami, Proc. Natl. Acad. Sci. USA **118**, e2021810118 (2021).

[13] S. Ninet, F. Datchi, P. Dumas, M. Mezouar, G. Garbarino, A. Mafety, C. J. Pickard, R. J. Needs, and A. M. Saitta, Phys. Rev. B **89**, 174103 (2014).

[14] T. Palasyuk, I. Troyan, M. Eremets, V. Drozd, S. Medvedev, P. Zaleski Ejgierd, E. Magos Palasyuk, H. Wang, S. A. Bonev, D. Dudenko, and P. Naumov, Nat. Commun. **5**, 3460 (2014).

[15] C. J. Pickard and R. J. Needs, Nat. Mater. **7**, 775 (2008).

[16] R. D. Dick, J. Chem. Phys. **74**, 4053 (1981).

[17] A. C. Mitchell and W. J. Nellis, J. Chem. Phys. **76**, 6273 (1982).

[18] H. B. Radousky, A. C. Mitchell, and W. J. Nellis, J. Chem. Phys. **93**, 8235 (1990).

[19] W. J. Nellis, N. C. Holmes, A. C. Mitchell, D. C. Hamilton, and M. Nicol, J. Chem. Phys. **107**, 9096 (1997).

[20] S. Ninet and F. Datchi, J. Chem. Phys. **128**, 154508 (2008).

[21] J. A. Queyroux, S. Ninet, G. Weck, G. Garbarino, T. Plisson, M. Mezouar, and F. Datchi, Phys. Rev. B **99**, 134107 (2019).

[22] F. Li, M. Li, Q. Cui, T. Cui, Z. He, Q. Zhou, and G. Zou, J. Chem. Phys. **131**, 134502 (2009).

[23] J. G. O. Ojwang, R. Stewart McWilliams, X. Ke, and A. F. Goncharov, J. Chem. Phys. **137**, 064507 (2012).

[24] F. Datchi, S. Ninet, M. Gauthier, A. M. Saitta, B. Canny, and F. Decremps, Phys. Rev. B **73**, 174111 (2006).

[25] D. Li, P. Zhang, and J. Yan, J. Chem. Phys. **139**, 134505 (2013).

[26] M. Bethkenhagen, M. French, and R. Redmer, J. Chem. Phys. **138**, 234504 (2013).

[27] G. Kresse and J. Furthmüller, Phys. Rev. B **54**, 11169 (1996).

[28] J. Sun, A. Ruzsinszky, and J. P. Perdew, Phys. Rev. Lett. **115**, 036402 (2015).

[29] S. Nosé, J. Chem. Phys. **81**, 511 (1984).

[30] N. D. Mermin, Phys. Rev. **137**, A1441 (1965).

[31] M. Millot, S. Hamel, J. R. Rygg, P. M. Celliers, G. W. Collins, F. Coppari, D. E. Fratanduono, R. Jeanloz, D. C. Swift, and J. H. Eggert, Nat. Phys. **14**, 297 (2018).

[32] See Supplemental Material at http://link.aps.org/supplemental/10.1103/PhysRevB.106.014108 for computational methods, data analysis, and supplemental Figs. S1-S7 and Table S1, which includes Refs. [1,26–31,35,41,43–60].

[33] M. Preising and R. Redmer, Phys. Rev. B **100**, 184107 (2019).

[34] H. Hirai, K. Konagai, T. Kawamura, Y. Yamamoto, and T. Yagi, Phys. Earth Planet. Inter. **174**, 242 (2009).

[35] M. Millot, F. Coppari, J. R. Rygg, A. Correa Barrios, S. Hamel, D. C. Swift, and J. H. Eggert, Nature (London) **569**, 251 (2019).

[36] R. Redmer, T. R. Mattsson, N. Nettelmann, and M. French, Icarus **211**, 798 (2011).

[37] R. L. Mills, D. H. Liebenberg, and P. Pruzan, J. Phys. Chem. **86**, 5219 (1982).

[38] F. Simon and G. Glatzel, Z. Anorg. Allg. Chem. **178**, 309 (1929).

[39] J. A. Queyroux, J. A. Hernandez, G. Weck, S. Ninet, T. Plisson, S. Klotz, G. Garbarino, N. Guignot, M. Mezouar, M. Hanfland, J. P. Itieé, and F. Datchi, Phys. Rev. Lett. **125**, 195501 (2020).

[40] M. A. Ricci, M. Nardone, F. P. Ricci, C. Andreani, and A. K. Soper, J. Chem. Phys. **102**, 7650 (1995).

[41] S. Sun, Y. He, D. Y. Kim, and H. Li, Phys. Rev. B **102**, 104108 (2020).

[42] M. French, M. P. Desjarlais, and R. Redmer, Phys. Rev. E **93**, 022140 (2016).

[43] J. A. Hernandez and R. Caracas, Phys. Rev. Lett. **117**, 135503 (2016).

[44] G. Kresse and D. Joubert, Phys. Rev. B **59**, 1758 (1999).

[45] M. Chen, H. Y. Ko, R. C. Remsing, M. F. C. Andrade, B. Santra, Z. Sun, A. Selloni, R. Car, M. L. Klein, J. P. Perdew, and X. Wu, Proc. Natl. Acad. Sci. USA **114**, 10846 (2017).

[46] J. Xu, C. Zhang, L. Zhang, M. Chen, B. Santra, and X. Wu, Phys. Rev. B **102**, 214113 (2020).

[47] G. Zhao, H. Wang, M. C. Ding, X. G. Zhao, H. Y. Wang, and J. L. Yan, Phys. Rev. B **98**, 184205 (2018).

[48] H. C. Yang, K. Liu, Z. Y. Lu, and H. Q. Lin, Phys. Rev. B **102**, 174109 (2020).

[49] S. Azadi and T. D. Kühne, Phys. Rev. B **100**, 155103 (2019).

[50] E. R. Meyer, J. D. Kress, L. A. Collins, and C. Ticknor, Phys. Rev. E **90**, 043101 (2014).

[51] J. Heyd, G. E. Scuseria, and M. Ernzerhof, J. Chem. Phys. **118**, 8207 (2003).

[52] R. Kubo, J. Phys. Soc. Jpn. **12**, 570 (1957).

[53] D. A. Greenwood, Proc. Phys. Soc. **71**, 585 (1958).

[54] Z. Q. Wang, Z. G. Li, Y. F. Wang, L. Liu, Y. J. Gu, Q. F. Chen, and X. R. Chen, Phys. Rev. E **100**, 033214 (2019).

[55] Z. Q. Wang, J. Tang, Y. Hou, Q. F. Chen, X. R. Chen, J. Y. Dai, X. J. Meng, Y. J. Gu, L. Liu, G. J. Li, Y. S. Lan, and Z. G. Li, Phys. Rev. E **101**, 023302 (2020).

[56] Z. Q. Wang, Y. J. Gu, Q. F. Chen, Z. G. Li, L. Liu, G. J. Li, Y. S. Lan, and X. R. Chen, Phys. Rev. B **103**, 014109 (2021).

[57] E. R. Hernández and J. Íñiguez, Phys. Rev. Lett. **98**, 055501 (2007).

[58] R. Paul, S. X. Hu, and V. V. Karasiev, Phys. Rev. Lett. **122**, 125701 (2019).

[59] A. Baldereschi, Phys. Rev. B **7**, 5212 (1973).

[60] G. J. Guo, Y. G. Zhang, K. Refson, and Y. J. Zhao, Mol. Phys. **100**, 2617 (2002).